Quantification of van der Waals forces in bimodal and trimodal AFM

Sergio Santos[1,*], Karim Gadelrab[2], Lamiaa Elsherbiny[3], Xaver Drexler[1], Tuza Olukan[1], Josep Font[4], Victor Barcons[4], Matteo Chiesa[1,3,**]

[1]UiT-the Arctic University of Norway, Department of Physics and Technology, 9037, Tromsø, Norway

[2]Department of Materials Science and Engineering, Massachusetts Institute of Technology, Cambridge, MA 02139, USA

[3]Laboratory for Energy and NanoScience (LENS), Khalifa University of Science and Technology, Masdar Institute Campus, 127788, Abu Dhabi, United Arab Emirates

[4]Departament d'Enginyeria Minera, Industrial i TIC, UPC BarcelonaTech, 08242 Manresa, Spain

Authors to whom correspondence should be addressed: *Sergio Santos, ssantos78h@gmail.com; **Matteo Chiesa, matteo.chiesa@ku.ac.ae

Abstract

The multifrequency formalism is generalized and exploited to quantify attractive forces, i.e., the van der Waals interactions, with small amplitudes or gentle forces in bimodal and trimodal AFM. The multifrequency force spectroscopy formalism with higher modes, including trimodal AFM, can outperform bimodal AFM for material property quantification. Bimodal AFM with the second mode is valid when the drive amplitude of the first mode is approximately an order of magnitude larger than that of the second mode. The error increases in the second mode but decreases in the third mode with decreasing drive amplitude ratio. Externally driving with higher modes provides a means to extract information of higher force derivatives while enhancing the range of parameter space where the multifrequency formalism holds. Thus, the present approach is compatible with robustly quantifying weak long range forces while extending the number of channels available for high resolution.

I. INTRODUCTION

Multifrequency atomic force microscopy (AFM) is a dynamic mode of AFM which enhances resolving power, provides extra contrast channels, and is equipped with a formalism to quantify material properties[1]. Since its inception, dynamic AFM (AFM) was divided into two main modes of operation, i.e., amplitude modulation[2] (AM) AFM and frequency modulation[3] (FM) AFM. In both approaches a microcantilever with a sharp tip at its end is excited at or near its resonant frequency. AM AFM tracks the amplitude decay while FM AFM tracks the frequency shift. The tracking parameter shaped the lines of research in each field. For example Giessibl[4, 5], Sader and Jarvis[6-8] derived a general expression relating the frequency shift to the tip-sample force during the late 90s and early 2000s. In the AM AFM field others focused on the relationships between the tip-sample force and the amplitude decay. For example, in 2001, San Paulo and García derived a generic expression based on the virial of the interaction and the energy dissipation expressions[9]. The virial of interaction, or virial, is the time averaged tip-sample force times displacement and accounts for the amplitude decay due to conservative forces. The virial, as concept in dynamic AFM, arguably brings together the above lines of research[10, 11]. Stark and others[12-14] reported the effects of higher harmonics to the dynamics of the cantilever and in the 2000s several methods that monitor higher harmonics and higher modes emerged. The reader can refer to Roger Proksch[15], Solares and Chawla[16] or García and Herruzo[1] for a brief introduction to the early developments. More recently, advances [17-19] include the work of Eichhorn and Dietz[20-22] where torsional and flexural modes are simultaneously excited and monitored and advances in the understanding of qPlus sensors [23, 24]. In this work we focus on bimodal AFM, as introduced in 2004[25] and 2006[15, 26], trimodal AFM as introduced in 2010[27], and the multifrequency formalism for force spectroscopy to quantify material properties[11, 28-35]. Here, van der Waals (vdW) forces are taken as a model force to be investigated in multifrequency AFM since these interactions are widely employed in current research[36] that could be impacted or exploited through our findings. For example, in the field of fabrication of nanostructures and nanodevices, vdW forces offer an alternative bond-free integration strategy without lattice and processing limitations[37]. In particular, in two-dimensional layered materials (2DLMs) weak vdW interactions are responsible for the integration of highly disparate materials without the constraints of crystal lattice matching[38]. The same principles are being exploited to move beyond two dimensional structures[37] and, amongst other[39, 40], also exploited in advanced nanophotonic and opto-electronic applications[41]. In short, in this study the vdW forces are parametrized in terms of the ubiquitous inverse square law[42] where the proportional parameter provides information regarding the magnitude of the force. The force spectroscopy expressions are then generalized to higher modes, including the simultaneous excitation of more than 2 modes, in order to investigate the sensitivity and robustness of the formalism.

II. MODEL

The dynamics of the AFM cantilever interacting with a surface can be reduced to a set of M governing equations[28], one equation representing each eigenmode i, expressed in terms of the standard linear differential equations employed to describe driven harmonic motion, with the addition of the tip-sample force F_{ts}

$$m\ddot{z}_i = -k_i z_i - \frac{m\omega_{0i}}{Q_i}\dot{z}_i + \sum_{i=1}^{i=M} F_{0i}\cos\omega_i t + F_{\mathrm{ts}}(\mathrm{z}) \qquad (1)$$

where m is the effective mass, k_i, Q_i and ω_{0i} are the spring constant, the Quality factor and the natural angular frequency of each mode i. M is the number of modes employed to model the system and/or where external driving forces are acting, F_{0i} and ω_i are the driving force and the driving angular frequency at or near the resonance of each mode and $F_{ts}(z)$ is the tip-sample force acting at the cantilever position z. The reduction of the dynamics to M equations is made under the assumption that the relevant information is mostly contained in these M eigenmodes at the frequencies of interest, i.e., those where there is a drive ω_i. Furthermore, z can be expressed in terms of the frequency components coinciding with the drive frequencies ω_i as follows

$$z(t) = \sum_{i=1}^{i=M} z_i + O(\varepsilon) \approx \sum_{i=1}^{i=M} A_i \cos(\omega_i t - \phi_i) \tag{2}$$

where $O(\varepsilon)$ is the term carrying the contributions of higher harmonics and higher modes, i.e., it is the error not accounted for by the higher modes at frequencies other than ω_i.[43] The amplitudes A_i and phases ϕ_i are experimental observables in multifrequency AFM. It follows that F_{ts} can be approximated to

$$F_{\mathrm{ts}}(\mathrm{z}) \approx F_{\mathrm{ts}}\left(\sum_{i=1}^{i=M} z_i\right) \tag{3}$$

Standard bimodal AFM typically employs the first two modes, i.e., m=1 and m=2, and was introduced in 2004. Trimodal AFM[44] was introduced in 2010 and the first three eigenmodes are excited at, or near, the natural frequency of oscillation. Here we reduce the system to M=3 and explore the consequences for the extraction of material properties when exciting the first, second and the third modes simultaneously as in trimodal, or, as in bimodal, two modes at a time. Furthermore, this study focuses on gentle interactions, i.e., roughly speaking the small amplitudes typically employed to image in the attractive regime in AM AFM[25, 30]. For this reason we employ the same model employed in the original study of 2004[25]

$$F_{ts} = -\frac{\alpha}{(z_c+z)^2} \qquad \text{where } d = z_c + z \quad \text{and} \quad d > a_0 \tag{4}$$

where z_c is the tip-sample rest separation[45], α dictates the magnitude of the phenomena[30] or the strength of the force[46], d is the instantaneous tip-sample distance and a_0 is an intermolecular distance introduced to avoid the divergence of (4) and physically represents matter impenetrability, i.e., the atoms on the tip and the atoms on the surface cannot be closer than a_0. Other details on the approximations and validity of (4) can be found elsewhere[45]. The expression in (4) is typically employed in AFM to model long range attractive, i.e., vdW, forces. It is perhaps more interesting to write (4) in terms of the Hamaker H and the tip radius R[42]. Then, α=RH/6. Since this work focuses on gentle forces the interactions of interest are $d>a_0$ throughout. Experimentally this can be achieved by employing sufficiently small amplitudes[30, 47]. The virials of interaction contain information about conservative forces such as those in (4). [9] The virials for each mode are defined as[28]

$$V_i = \langle F_{ts} z_i \rangle = \frac{1}{T}\int_0^T F_{ts} z_i dt \tag{5}$$

These expressions can be expressed in terms of experimental observables by noting that combining (1) and (2) and integrating over a full cycle

$$V_i = -\frac{1}{2} F_{0i} A_i cos\phi_i \tag{6}$$

where, at the resonances, $F_{0i}= k_iA_{0i}/Q_i$. Thus, all the terms in (6) can be experimentally calibrated or monitored. In principle, extracting the sample's parameters consists in inserting a model in (5) and solving the integrals. A constraint is that there must be as many equations (5), i.e., modes M, as unknowns in the model. In (4) the unknowns are two, i.e., z_c and α. For the virial of the first mode, i.e., the fundamental frequency ω_{01} with period T, the following approximation simplifies the solution[30, 47]

$$V_1 = \langle F_{ts} z_1 \rangle = \frac{1}{T}\int_0^T F_{ts} z_1 dt \approx -\frac{1}{T}\int_0^T \frac{\alpha}{(z_c+z_1)^2} z_1 dt \tag{7}$$

The approximation in (7) is valid provided the amplitude of the first mode A_1 is much larger than the amplitudes of the higher modes, i.e., $z \approx z_1$. The solution of (7) was already provided in 2001 by the authors that introduced the virial theorem in AFM[9]

$$V_1(n=2) \approx \frac{\alpha}{A_1}\left[\left(\frac{z_c}{A_1}\right)^2 - 1\right]^{-3/2} \tag{8}$$

Combining (6) and (8) is not sufficient to extract α since there are two unknowns, i.e., α and z_c. By exciting the second mode, i.e., bimodal, another equation is available, albeit the approximation in (7) for higher modes is too cumbersome. A more manageable approximation was later introduced where[48, 49]

$$V_2 \approx \frac{A_2^2}{2}\frac{1}{T}\oint \frac{\partial F_{ts}}{\partial \mathrm{d}} dt \tag{9}$$

Here, we propose using (9) for higher modes. Thus we proceed to expand the formalism to extract material properties using (9) for any higher mode or combination of higher modes where

$$V_i \approx \frac{A_i^2}{2}\frac{1}{T}\oint \frac{\partial F_{ts}}{\partial \mathrm{d}} dt \qquad \text{for i= 2, 3, …} \tag{10}$$

Inserting (4) into (10)

$$V_i(n=2) \approx \alpha \left[\frac{A_i}{A_1}\right]^2 \frac{1}{A_1}\left[\left(\frac{z_c}{A_1}\right)^2 + \frac{1}{2}\right]\left[\left(\frac{z_c}{A_1}\right)^2 - 1\right]^{-5/2} \tag{11}$$

where n= 2 is a reminder of the power in (4) while (6), (8) and (11) can be combined to express the unknowns in (4) (z_c and α) in terms of observables

$$z_c = A_1 \left(\frac{1+b/2}{1-b}\right)^{1/2} \tag{12}$$

$$\alpha = A_1 V_1 \left[\left(\frac{z_C}{A_1}\right)^2 - 1\right]^{3/2} \; or\ alternatively, \alpha = A_1 V_1 \left[\left(\frac{1+b/2}{1-b}\right) - 1\right]^{3/2} \tag{13}$$

where

$$b_i = \left[\frac{A_i}{A_1}\right]^2 \frac{V_1}{V_i} \tag{14}$$

It follows that z_c and α can be written in terms of observables by exciting modes 1 and 2, modes 1 and 3 or modes 1, 2 and 3 simultaneously. If higher modes were excited the same equations would still hold since the contribution from the modes is contained in the subscript of (14). If three modes are simultaneously excited approximations for α and z_c can be found from modes 1 and 2 and modes 1 and 3 simultaneously. Finally, the minimum distance of approach d_m is more meaningful as a parameter than z_c in terms of the interaction, i.e., d_m is the minimum distance between the tip and the sample during an oscillation cycle. Thus, we propose two approximations for d_m that result from (12) as follows

$$d_m = A_1 \left[\sqrt{\frac{1+b/2}{1-b}} - 1\right] \text{where } d_m \approx z_c - A_1 \tag{15}$$

$$d_m = A_1\left[\sqrt{\frac{1+b/2}{1-b}} - \frac{\sum_{i=1}^{i=M} A_i}{A_1}\right] \text{ where } d_m \approx z_c - (A_1 + A_2 + A_3) \tag{16}$$

The approximation in (15), i.e., $d_m \approx z_c - A_1$, is the standard approximation[48, 50] in multifrequency AFM. The approximation in (16), i.e., $d_m \approx z_c - (A_1+A_2+\ldots+A_M)$, is introduced here to improve the results as discussed later.

III. RESULTS

A comparison between the virials as expressed in (5), and as obtained from numerically integrating the equations of motion, and the approximation to the virials in Eqs. (8) and (10) for the first and higher modes respectively, is shown in FIG. 1. The parameters used for the simulations are given in the figure caption. The top panels (a to c) show the results for virials 1, 2 and 3 when only the first and second modes are excited. The bottom panels (d to f) show the results for virials 1, 2 and 3 when only the first and third modes are excited. The first mode was excited with a free amplitude of $A_{01} = 2$nm throughout. The higher modes were excited with amplitudes of 0.2 nm. The numerical results obtained directly from Eq. (5) are shown in black squares and the approximations from Eq. (10) are shown in blue circles. The virials are shown as a function of the normalized fundamental amplitude A_1/A_{01} since this is the target amplitude typically employed as feedback. In the presence of external drive (a and b and d and f) the approximations hold. In particular, at higher set-points, i.e., $A_1/A_{01} > 0.2$-0.4, the errors are $\sim$ 10% or less and improve with increasing set-point both when exciting the second (FIG. 1b) and the third modes (FIG. 1f). This is consistent with our latest reports[30]. The expressions for the virials (Eq. 11) when there is no external excitation in the higher modes (FIGS. 1c and 1e) cannot be employed since the errors are too large. The reasoning is that without external drive the expression in (6) is zero, i.e., the assumptions of multifrequency do not hold.

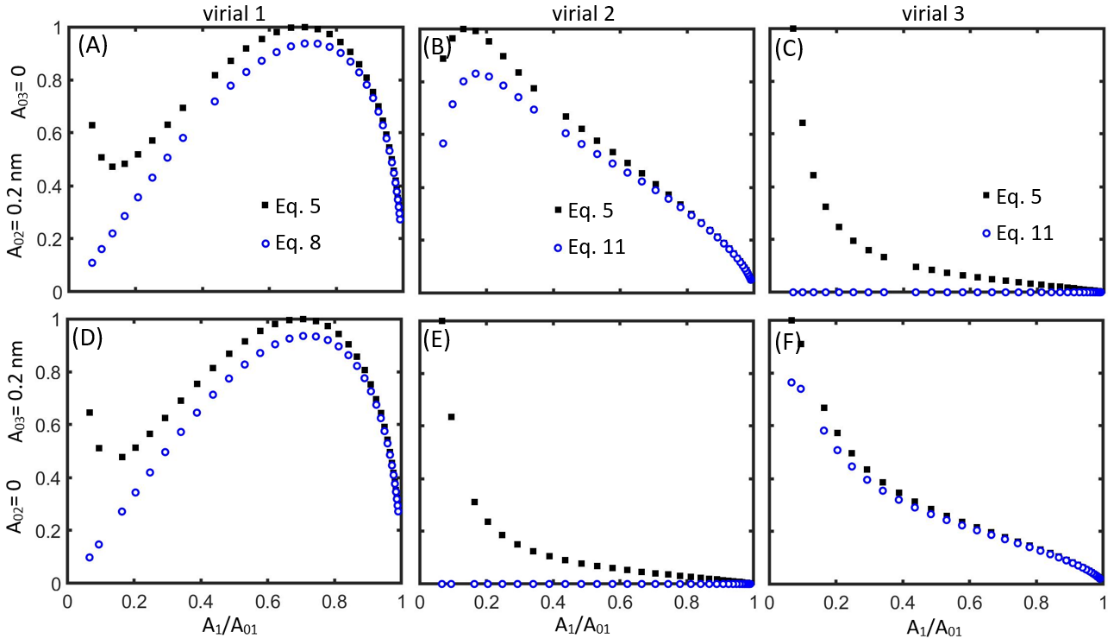

FIG. 1. Bimodal AFM where either modes 1 and 2 (a, b, and c) or modes 1 and 3 (d, e, and f) are externally excited. The virial expressed as a time integral of the displacement weighted tip sample force (Eq. 5) is shown in black squares as directly computed from the numerical integration of the equations of motion and the approximations in Eqs. 8 (virial 1) and 11 (virials 2 or 3 since the same expression applies for both). Where there is no external drive the approximation in Eq. 11 is invalid as shown from inspecting panels c and e. The parameters in the simulations for each mode are k_1= 2 N/m, k_2= 80 N/m, k_3= 600 N/m, f_{01}= 70kHz (ω01=2π f_{01}), f_{02}= 420kHz, f_{03}= 1190 kHz, Q_1 =100, Q_2 = 600 and Q_3 = 1800. For the physical parameters the values are R= 20 nm, a_0 = 0.165 nm and H=4.1x10^{-20} J. The virials are further normalized in relation to the maximum value of the numerical results with V_1 = 2x10^{-20} J, V_2 = 1.4x10^{-21} J, and V_3 = 3.4x10^{-21} J in the presence of external drive and V_2 = 2.6x10^{-22} J and V_3 = 3.4x10^{-23} J in the absence of external drive (panels c and e). The drives were A_{01}= 2nm, A_{02}= 0.2 nm A_{03} = 0 nm (top panels) and A_{02}= 0 nm A_{03} = 0.2 nm (bottom panels).

The results and discussion of FIG. 1 and the presence of the drive in the virial (Eq. 6) show that the multifrequency formalism can be exploited to recover relevant parameters provided there is an external drive in at least one higher mode. Here, Eqs. 12, 13, 15 and 16 have been employed to extract z_c, d_m and α in FIG. 2. The parameters of the simulations in FIG. 2 are the same as those in FIG. 1. Panels a and b in FIG. 2 show that z_c can be recovered relatively well for a range of set points above 0.2, i.e., A_1/A_{01}, in bimodal AFM by exciting modes 1 and 2 or 1 and 3. The behaviour is to be contrasted with the results of the virial approximations where the errors monotonically increase with decreasing set-point[30] throughout (Fig. 1). The practical significance is that driving at set-points above 0.2 - 0.4, i.e., $A_1/A_{01}>$ 0.2-0.4, leads to a valid approximation in multifrequency with regards to z_c (Eq. 12). Furthermore, for the operational parameters employed to generate the data in FIG. 2 the results are slightly better when using modes 1 and 2 than when using modes 1 and 3 (compare FIG. 2a with 2b). Our simulations show that decreasing the driving ratios, i.e., A_{01}/A_{02} or A_{01}/A_{03}, changes this trend (see FIG. 3 and discussion of FIG. 3). Panels c and d in FIG. 2 show the results for d_m. The two approximations for d_m are plotted with Eq. 15 in blue circles and Eq. 16 in red triangles. The same trend is found but the approximation from Eq. 16 is superior to that of Eq. 15. The results of recovering α (Eq. 13) are shown in FIGs. 2e and 2f for modes 1 and 2 and modes 1 and 3 respectively. Again the approximation is better when using modes 1 and 2 and the recovered value of α diverges as A_1/A_{01} tends to 1. It is worth mentioning however that the amplitude of the third mode A_3 does not significantly decrease, i.e., ~ 1 pm, at high set-points, i.e., $A_1/A_{01}>$ 0.9. The numerical values for z_c, dm and α for the data in Fig. 2 are shown in Table I and II for some relevant values of A_1/A_{01} for bimodal operated with modes 1 and 2 (Figs. 2a, 2c and 2e) and modes 1 and 3 (Figs. 2b, 2d and 2f) respectively. Errors for z_c, d_m and α are also provided.

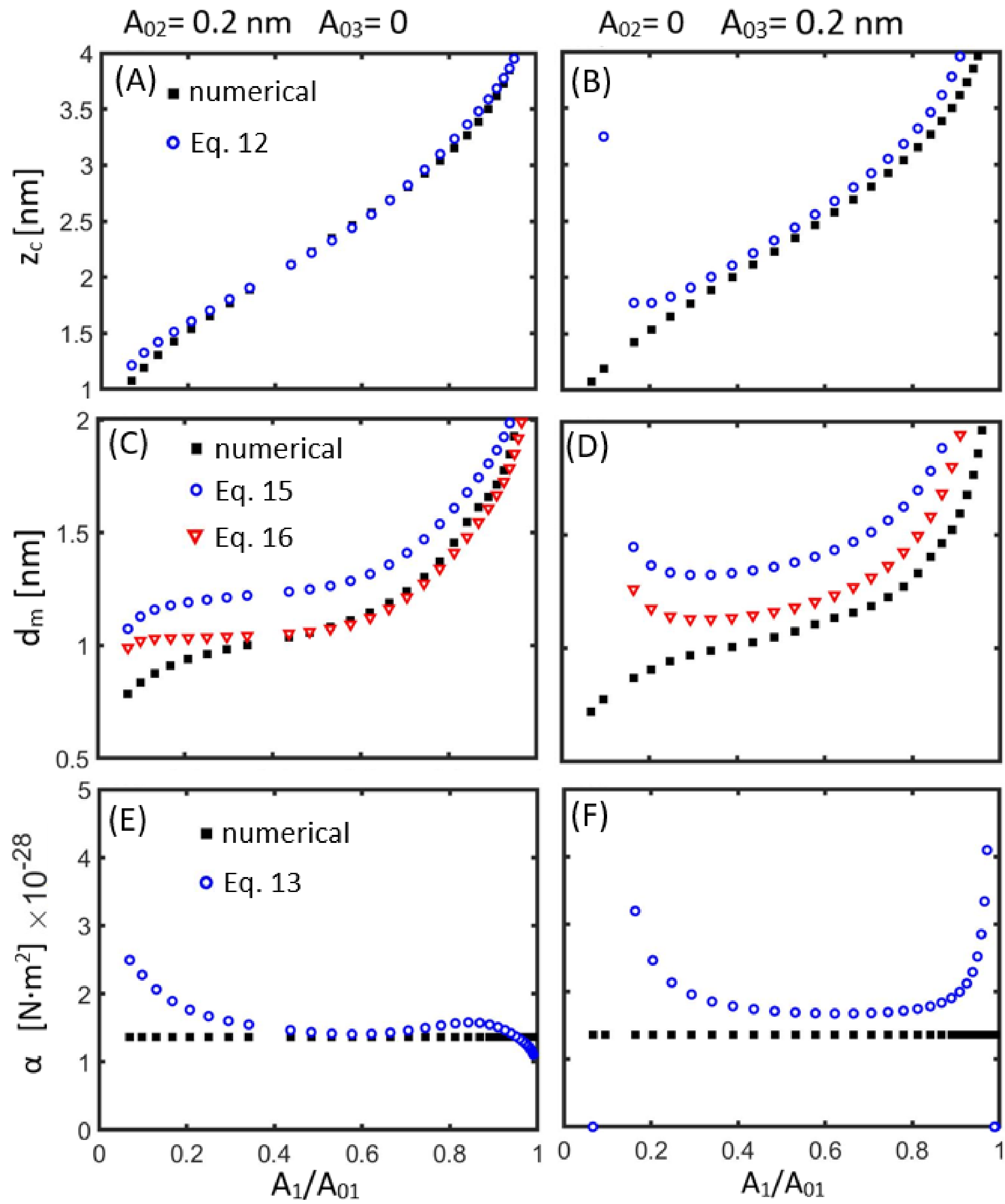

FIG. 2. Comparison of bimodal AFM where either modes 1 and 2 (left panels) or modes 1 and 3 (right panels) are externally excited. The black squares show the values obtained directly from numerical results and the blue circles show the values obtained from the approximations in Eq. 12 (a and b) for the cantilever separation z_c, Eq. 15 (c and d) for the minimum distance of approach d_m, and Eq. 13 (e and f) for α in Eq. 4. The red triangles

in panels c and d show the approximation for d_m in Eq. 16. The rest of parameters are the same as those in FIG. 1. Since α is a constant in the simulations, it takes on a single value for the whole range of set points A_1/A_{01}.

A_1/A_{01}	z_c [nm]	error z_c [pm]	d_m [nm]	error d_m [pm]		α [N·m²] x10⁻²⁸	error α x10⁻²⁸ [N·m²]
				Eq. 15	Eq. 16		
0.95	3.96	-12	1.93	122	-77	1.37	0.01
0.9	3.5	88	1.66	149	-50	1.37	0.18
0.85	3.27	94	1.55	132	-66	1.37	0.21
0.8	3.15	81	1.45	154	-43	1.37	0.2
0.75	2.92	36	1.3	169	-28	1.37	0.13
0.7	2.81	13	1.24	169	-27	1.37	0.09
0.65	2.69	-5	1.19	169	-26	1.37	0.06
0.6	2.58	-17	1.15	171	-23	1.37	0.04
0.55	2.35	-20	1.08	183	-8	1.37	0.05
0.5	2.23	-13	1.06	192	3	1.37	0.07
0.45	2.12	-4	1.04	201	16	1.37	0.1
0.4	2.12	-4	1.04	201	16	1.37	0.1
0.35	1.88	20	1	220	41	1.37	0.18
0.3	1.77	34	0.98	229	55	1.37	0.23
0.25	1.65	49	0.96	239	72	1.37	0.3
0.2	1.54	68	0.94	251	94	1.37	0.39

Table I. Numerical values for z_c, d_m and α for the data in Figs. 2a, 2c and 2e (bimodal operated via modes 1 and 2) for some relevant values of A_1/A_{01}. The corresponding errors for z_c (Eqs. 12) , d_m (Eqs. 15 and 16) and α (Eq. 13) are also provided.

A_1/A_{01}	z_c [nm]	error z_c [pm]	d_m [nm]	error d_m [pm]		α [N·m^2] x10^{-28}	error α x10^{-28} [N·m^2]
				Eq. 15	Eq. 16		
0.95	3.96	681	1.86	885	684	1.37	1.15
0.9	3.62	342	1.59	546	346	1.37	0.63
0.85	3.27	194	1.4	380	179	1.37	0.42
0.8	3.15	166	1.33	365	164	1.37	0.38
0.75	2.92	128	1.22	339	138	1.37	0.33
0.7	2.81	116	1.19	325	125	1.37	0.32
0.65	2.69	107	1.16	312	112	1.37	0.31
0.6	2.58	100	1.14	298	98	1.37	0.31
0.55	2.35	95	1.07	304	105	1.37	0.32
0.5	2.23	96	1.05	310	112	1.37	0.34
0.45	2.12	99	1.03	317	119	1.37	0.37
0.4	2	107	1.01	324	127	1.37	0.42
0.35	1.88	120	0.99	336	140	1.37	0.48
0.3	1.77	141	0.97	356	161	1.37	0.59
0.25	1.65	175	0.94	392	198	1.37	0.77
0.2	1.54	236	0.91	458	267	1.37	1.1

Table II. Numerical values for z_c, d_m and α for the data in Figs. 2b, 2d and 2f (bimodal operated via modes 1 and 3) for some relevant values of A_1/A_{01}. The corresponding errors for z_c (Eqs. 12) , d_m (Eqs. 15 and 16) and α (Eq. 13) are also provided.

FIG. 3 shows a direct comparison between the recovery of z_c, d_m and α from modes 1 and 2 (blue circles) and modes 1 and 3 (red triangles). Again, this is contrasted to numerical results (black squares). The panels on the left (FIGs. 2a, 2c and 2e) show the behaviour when the ratio of drives is 10 %, i.e., A_{02}/A_{01} =0.1 and A_{03}/A_{01} =0.1 for modes 1 and 2 and 1 and 3 respectively. The panels on the right (FIGs. 2b, 2d and 2f) show the behaviour when the ratio of drives is 2.5% %, i.e., A_{02}/A_{01} =0.025 and A_{03}/A_{01} =0.025 for modes 1 and 2 and 1 and 3 respectively. The interpretation of the results is the same as that given for FIG. 2 but a comparison between the left and right panels shows that as the ratio of drives decreases the errors increase when driving with the first and second modes and improves when driving with the first and third modes. This result could be understood when considering that Eq. 10 was derived by considering that the higher mode frequency is much larger Simulations show that by further decreasing the drive ratios to 0.01 the trend improves for the first and third modes and worsens for modes 1 and 2 (data not shown). The practical implication is that in bimodal AFM, and for the recovery of material properties in multifrequency AFM, the driving ratio should be maintained at approximately 10% when driving with the first and second modes while it can be significantly decreased when driving with the first and third modes. Since the resolution might be better when driving with smaller amplitudes this provides a means to extracting material properties with smaller higher mode amplitudes without compromising contrast. The results also extend the applicability of bimodal AFM for the extraction of material properties for driving ratios below 10%. We recently discussed that the 10% ratio is optimal in bimodal AFM for modes 1 and 2[30, 48]. The numerical values for z_c, d_m and α for the data in Fig. 3 are shown in Table III for some relevant values of A_1/A_{01} for bimodal operated with modes 1 and 2 and modes 1 and 3 (Figs. 2a, 2c and 2e) with higher mode amplitudes of 200 pm. In and IV (Figs. 2b, 2d and 2f) the results when driving with higher mode amplitudes of 50 pm are provided. The errors for z_c, d_m and α are shown in both tables as in Tables I and II. Finally, a discussion of the results obtained when driving the three modes simultaneously, for the recovery of material properties, and according to the above formalism, is given below with the help of FIG. 4.

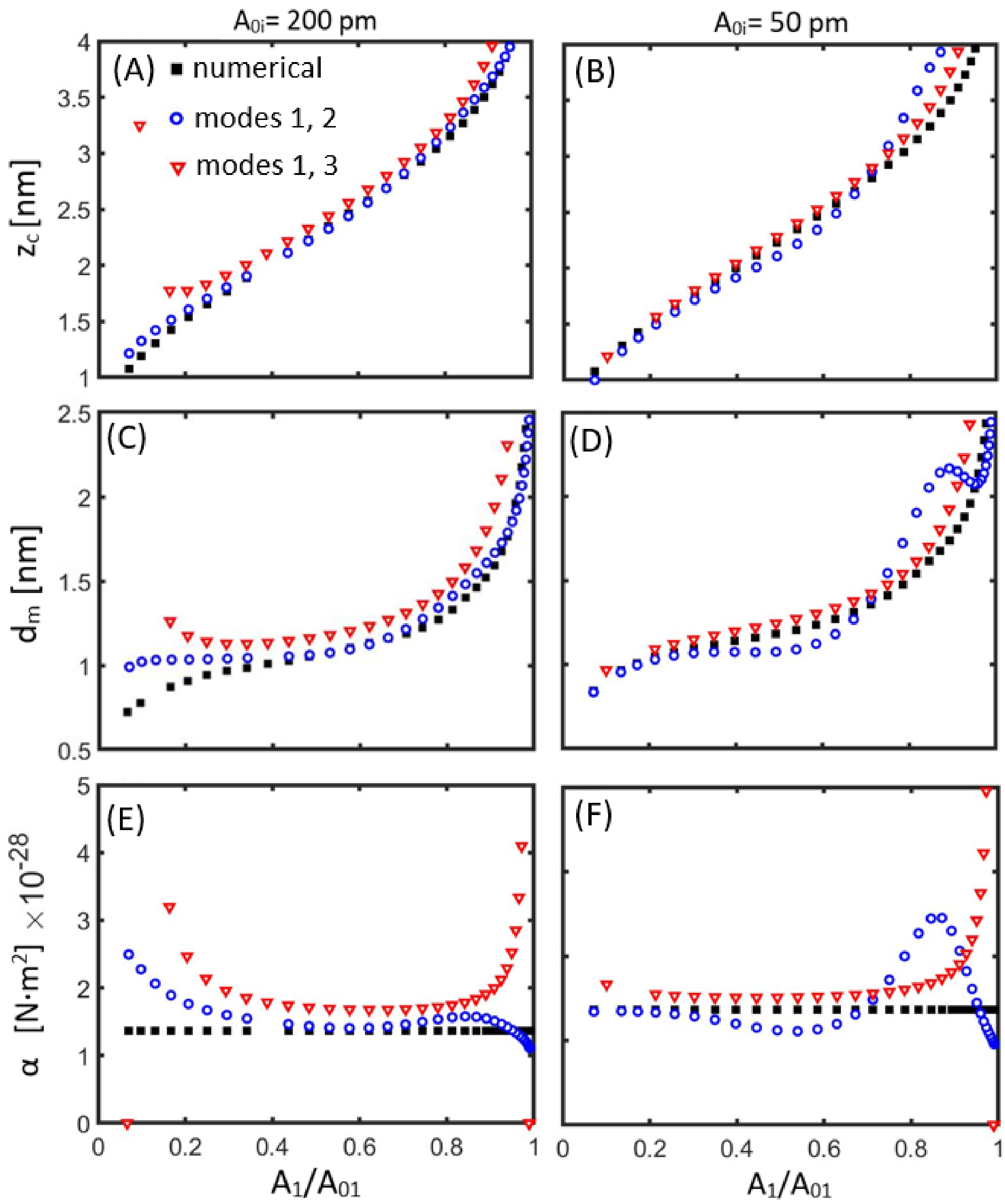

FIG. 3. Comparison of bimodal AFM where either modes 1 and 2 (blue circles) or modes 1 and 3 (red triangles) are externally excited. The black squares show the values obtained directly from numerical results. For the left panels the drive amplitudes are A_{01}= 2 nm and 0.2 nm for the externally excited higher mode, otherwise 0. For the right panels the drive amplitudes are A_{01}= 2 nm and 0.05 nm for the externally excited higher mode, otherwise 0. The figures show a comparison for the extraction of z_c (a and b), d_m (c and d) and α (e and f) respectively with different drive ratios. The rest of parameters are the same as those in FIG. 1.

A_1/A_{01}	z_c [nm]		error z_c [pm]		d_m [nm]		error d_m [pm]		α [N·m^2] x10^{-28}	error α [N·m^2] x10^{-28}	
	m1,m2	m1,m3	m1,m2	m1,m3	m1,m2	m1,m3	m1,m2	m1,m3		m1,m2	m1,m3
0.95	3.96	3.96	-12	681	1.93	1.86	-77	684	1.37	0.01	1.15
0.9	3.5	3.62	88	342	1.66	1.59	-50	346	1.37	0.18	0.63
0.85	3.27	3.27	94	194	1.55	1.4	-66	179	1.37	0.21	0.42
0.8	3.15	3.15	81	166	1.45	1.33	-43	164	1.37	0.2	0.38
0.75	2.92	2.92	36	128	1.3	1.22	-28	138	1.37	0.13	0.33
0.7	2.81	2.81	13	116	1.24	1.19	-27	125	1.37	0.09	0.32
0.65	2.69	2.69	-5	107	1.19	1.16	-26	112	1.37	0.06	0.31
0.6	2.58	2.58	-17	100	1.15	1.14	-23	98	1.37	0.04	0.31
0.55	2.35	2.35	-20	95	1.08	1.07	-8	105	1.37	0.05	0.32
0.5	2.23	2.23	-13	96	1.06	1.05	3	112	1.37	0.07	0.34
0.45	2.12	2.12	-4	99	1.04	1.03	16	119	1.37	0.1	0.37
0.4	2.12	2	-4	107	1.04	1.01	16	127	1.37	0.1	0.42
0.35	1.88	1.88	20	120	1	0.99	41	140	1.37	0.18	0.48
0.3	1.77	1.77	34	141	0.98	0.97	55	161	1.37	0.23	0.59
0.25	1.65	1.65	49	175	0.96	0.94	72	198	1.37	0.3	0.77
0.2	1.54	1.54	68	236	0.94	0.91	94	267	1.37	0.39	1.1

Table III. Numerical values for z_c, d_m and α for the data in Figs. 3a, 3c and 3e in bimodal operated via modes 1 and 2 (m1, m2) and modes 1 and 3 (m1, m3) respectively for some relevant values of A_1/A_{01}. The higher mode drive amplitudes are 200 pm throughout. The corresponding errors for z_c (Eqs. 12) , d_m (16) and α (Eq. 13) are also provided. Values for errors in d_m and α are highlighted where trimodal AFM outperforms bimodal AFM for the same drive amplitudes (compare with table V).

A_1/A_{01}	z_c [nm]		error z_c [pm]		d_m [nm]		error d_m [pm]		α [N·m^2] x10^{-28}	error α [N·m^2] x10^{-28}	
	m1,m2	m1,m3	m1,m2	m1,m3	m1,m2	m1,m3	m1,m2	m1,m3		m1,m2	m1,m3
0.95	3.96	3.96	63	657	2.05	2.01	28	660	1.37	0.08	1.06
0.9	3.5	3.5	501	258	1.74	1.67	428	257	1.37	0.93	0.44
0.85	3.27	3.27	523	172	1.61	1.54	437	157	1.37	1.08	0.31
0.8	3.04	3.04	303	121	1.47	1.41	249	127	1.37	0.63	0.23
0.75	2.92	2.92	170	103	1.41	1.36	131	113	1.37	0.35	0.21
0.7	2.81	2.81	55	89	1.36	1.32	31	99	1.37	0.11	0.19
0.65	2.58	2.58	-89	69	1.27	1.27	-90	69	1.37	-0.17	0.16
0.6	2.46	2.46	-120	61	1.24	1.24	-113	61	1.37	-0.24	0.15
0.55	2.35	2.35	-130	55	1.21	1.21	-117	64	1.37	-0.26	0.14
0.5	2.23	2.23	-123	49	1.18	1.18	-106	65	1.37	-0.25	0.14
0.45	2.12	2.12	-106	45	1.16	1.16	-87	64	1.37	-0.22	0.14
0.4	2	2	-86	41	1.14	1.14	-65	61	1.37	-0.17	0.14
0.35	1.88	1.88	-67	37	1.12	1.12	-45	58	1.37	-0.12	0.14
0.3	1.77	1.77	-52	34	1.1	1.09	-30	54	1.37	-0.08	0.15
0.25	1.65	1.65	-45	30	1.07	1.07	-20	52	1.37	-0.05	0.16
0.2	1.54	1.54	-42	27	1.04	1.03	-15	57	1.37	-0.04	0.18

Table IV. Numerical values for z_c, d_m and α for the data in Figs. 3b, 3d and 3f in bimodal operated via modes 1 and 2 (m1, m2) and modes 1 and 3 (m1, m3) respectively for some relevant values of A_1/A_{01}. The higher mode drive amplitudes are 50 pm throughout. The corresponding errors for z_c (Eqs. 12), d_m (16) and α (Eq. 13) are also provided.

The data and discussion of FIGs. 1-3 focus on the behaviour of the cantilever and quantification in bimodal AFM by simultaneously exciting the first mode and the second or the third modes respectively. In FIG.4 results are shown for the simultaneous excitation of modes 1 to 3, i.e., trimodal AFM. First, the formalism above requires two equations (Eqs. 8 and 11) to solve for the two unknowns z_c and α in Eq. 4. While d_m is also an unknown, the equation for d_m (Eqs. 15 or 16) follows from geometric considerations alone based on z_c. The practical implication is that in trimodal AFM, provided there are two unknowns, i.e., here z_c and α, the unknowns can be recovered from 1) the dynamics of modes 1 and 2, 2) the dynamics of modes 1 and 3 or 3) from modes 1 and 2 and modes 1 and 3 simultaneously. The third possibility does not necessarily lead to inconsistency or redundancy since we are dealing with approximations. In this sense, quantifying parameters from multiple compatible sources can be used to confirm or establish the validity of the results. Second, since the second and third modes do not necessarily provide the same contrast while imaging[27, 44], the acquisition of contrast images from higher modes can be performed simultaneously with material properties quantification. For example, in FIG 4a the mean cantilever separation z_c recovered from the dynamics of the first and third modes (red triangles) is correct down to fractions of angstrom for relevant imaging conditions, i.e., $0.4 < A_1/A_{01} < 0.8$, and slightly outperforms the recovery carried out from modes 1 and 2 (blue circles). Furthermore, the first and second modes provide better results than the first and third modes at the extremes, i.e. $0.2 < A_1/A_{01}$ or $A_1/A_{01} > 0.9$. The same conclusions hold for the recovery of d_m (FIG. 4b) and α (FIG. 4c). The implication is that both channels, i.e., the second mode and third mode channels, can be simultaneously employed for contrast or material property quantification. Table V provides some numerical data relevant to Fig. 4. It is worth noting that the expression in Eq. 4 involves an inverse square law, i.e., the power is 2. But other power laws might be of interest in surface force characterization[51-53]. In this respect our simulations show (data not shown) that the above formalism is still valid when higher powers are employed, i.e., $F_{ts} \propto d^{-3}$, even though errors in z_c, d_m and α slightly increase. In particular, the higher the slope in the force profile the larger the error. This could be due to the fact that a Taylor expansion is employed when deriving Eq. 9 where only the first terms, i.e., first derivative, are kept[30, 48].

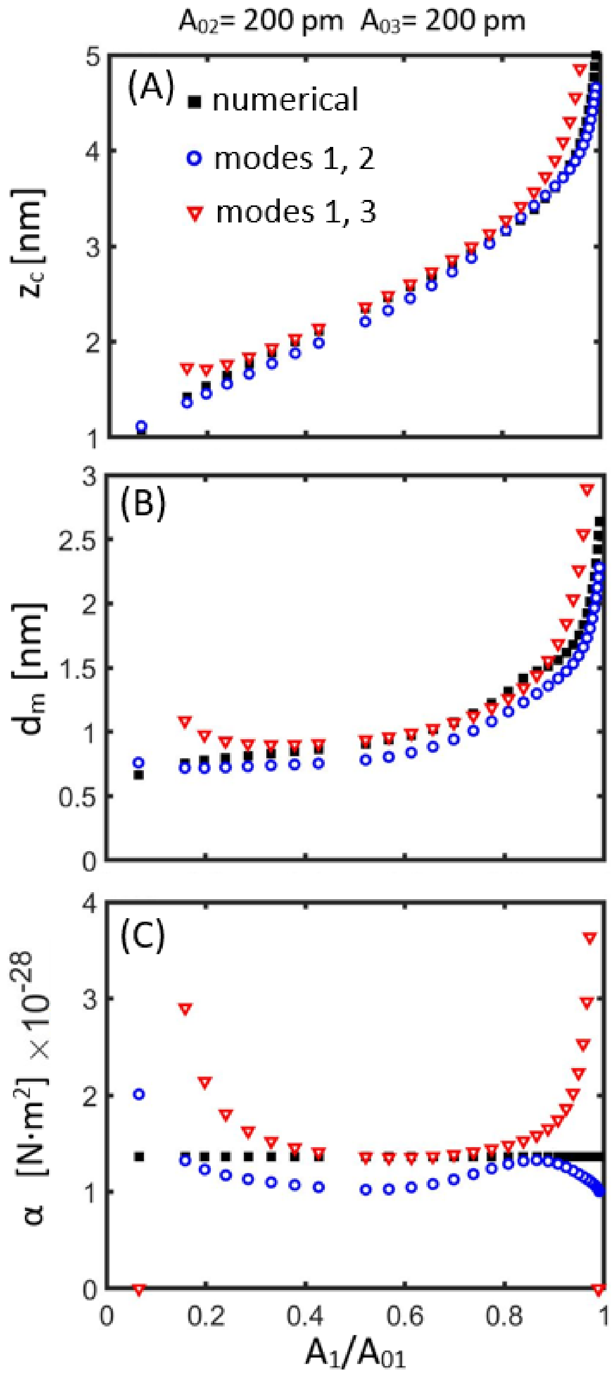

FIG. 4. Trimodal AFM where modes 1, 2 and 3 are simultaneously excited. The parameters z_c (a) , d_m (b) and α (c) can be simultaneously recovered from either modes 1 and 2 (blue circles) or 1 and 3 (red triangles). The black squares are obtained directly from the simulations as before. Eqs. 12, 13 and 16 have been used to recover z_c, α and d_m respectively. The rest of parameters are the same as those in FIG. 1.

A_1/A_0	z_c [nm]	error z_c [pm]		d_{min} [nm]	error d_{min} [pm]		α [N·m^2] x10^{-28}	error α [N·m^2] x10^{-28}	
		m1,m2	m1,m3		m1,m2	m1,m3		m1,m2	m1,m3
0.95	3.96	-72	596	1.75	-161	507	1.37	-0.18	0.87
0.9	3.62	14	285	1.56	-142	130	1.37	-0.08	0.38
0.85	3.27	34	147	1.42	-187	-73	1.37	-0.05	0.16
0.8	3.15	15	118	1.31	-157	-54	1.37	-0.08	0.11
0.75	2.92	-45	72	1.14	-135	-19	1.37	-0.18	0.04
0.7	2.81	-77	54	1.08	-135	-4	1.37	-0.24	0.02
0.65	2.69	-103	40	1.02	-135	7	1.37	-0.29	0
0.6	2.58	-122	29	0.97	-134	17	1.37	-0.32	-0.01
0.55	2.46	-133	23	0.94	-131	25	1.37	-0.34	-0.01
0.5	2.35	-136	20	0.91	-124	32	1.37	-0.34	-0.01
0.45	2.12	-127	26	0.86	-108	46	1.37	-0.32	0.04
0.4	2	-119	36	0.85	-99	56	1.37	-0.3	0.09
0.35	1.88	-111	50	0.83	-92	70	1.37	-0.27	0.16
0.3	1.77	-103	73	0.81	-84	92	1.37	-0.24	0.26
0.25	1.65	-94	111	0.8	-74	130	1.37	-0.2	0.44
0.2	1.54	-81	178	0.78	-60	198	1.37	-0.14	0.78

Table V. Numerical values for z_c, d_m and α for the data in Fig. 4 for some relevant values of A_1/A_{01} in trimodal AFM where the unknowns can be recovered from modes 1 and 2 (m1, m2) and/or modes 1 and 3 (m1, m3) respectively. The higher mode drive amplitudes are 200 pm throughout for modes 2 and 3. The corresponding errors for z_c (Eqs. 12) , d_m (16) and α (Eq. 13) are also provided. Values for errors in d_m and α are highlighted where trimodal AFM outperforms bimodal AFM for the same drive amplitudes (compare with table III).

IV. CONCLUSION

In summary, we have shown that the multifrequency formalism can be employed to extract material properties from the dynamics of the cantilever by exciting modes 1 and 2, 1 and 3 or 1, 2 and 3 simultaneously. The multifrequency approximation for force spectroscopy for higher modes (Eq. 10) seems to be universal since it states that the virial of any higher mode is proportional to the square of the amplitude of the mode times the time integral of the derivative of the force. The approximation can improve for higher modes, especially when small higher mode amplitudes are employed, i.e., $A_{0i}/A_{01} << 0.1$ for $i > 2$, while the same approximation is optimum when, and limited to, $A_{02}/A_{01} \approx 0.1$ for modes 1 and 2. Perhaps counterintuitively, the approximations to quantify material properties, i.e., the multifrequency formalism for force spectroscopy, in trimodal AFM might outperform bimodal AFM since the addition of higher modes does not seem to have a negative impact but rather the opposite. Furthermore, material property quantification in multifrequency AFM can improve irrespectively of the trends in the errors in the virial expressions. These results could be exploited in the expanding field of nanofabrication of materials and devices or nanophotonic biosensing[54] via van der Waals interactions[36, 41]. Finally, future studies could focus on extracting an arbitrary number of parameters M form M modes, i.e., M equations for M unknowns. The idea is that a model with an arbitrary number M of unknowns can always be solved by externally exciting M modes and exploiting the multifrequency method. The challenge is to find integrals such as those in Eqs. 7 and 10 that can be solved analytically. An example would be to extract the power law from Eq. 4 together with z_c and α.

AUTHOR DECLARATIONS

Conflict of Interest

The authors have no conflicts to disclose.

1. R. Garcia and E. T. Herruzo, Nature Nanotechnology **7** (4), 217-226 (2012).
2. R. García and R. Perez, Surface science reports **47** (6), 197-301 (2002).
3. F. J. Giessibl, Reviews of modern physics **75** (3), 949 (2003).
4. F. J. Giessibl, Physical Review B **56** (24), 16010 (1997).
5. F. J. Giessibl and H. Bielefeldt, Physical Review B **61** (15), 9968-9971 (2000).
6. J. E. Sader and S. P. Jarvis, Applied Physics Letters **84** (10), 1801-1803 (2004).
7. J. E. Sader and S. P. Jarvis, Physical Review B **70** (1), 012303 (2004).
8. J. E. Sader, T. Uchihashi, M. J. Higgins, A. Farrell, Y. Nakayama and S. P. Jarvis, Nanotechnology **16** (3), S94 (2005).
9. Á. S. Paulo and R. García, Physical Review B **64** (19), 193411 (2001).
10. A. J. Katan, M. H. Van Es and T. H. Oosterkamp, Nanotechnology **20** (16), 165703 (2009).
11. B. Rajabifar, A. Bajaj, R. Reifenberger, R. Proksch and A. Raman, Nanoscale **13** (41), 17428-17441 (2021).
12. R. W. Stark, T. Drobek and W. M. Heckl, Applied Physics Letters **74** (22), 3296-3298 (1999).
13. R. W. Stark, Nanotechnology **15** (3), 347 (2004).
14. A. Voss, C. Dietz, A. Stocker and R. W. Stark, Nano Research (2015).
15. R. Proksch, Applied Physics Letters **89**, 113121–113123 (2006).
16. S. D. Solares and G. Chawla, Journal of Applied Physics **108**, 054901 (2010).
17. M. Damircheli, U. Jung and R. Wagner, Physica Scripta **98** (3), 035708 (2023).
18. Q. Zeng, C. Sim, A. M. Yong, H. K. Hui, Y. Chen, L. Zhang, C. K. I. Tan, H. Liu and K. Zeng, Journal of Applied Physics **133** (4), 040901 (2023).
19. A. Alibakhshi, H. Jafari, A. A. Rostam-Alilou, M. Bodaghi and R. Sedaghati, Sensors and Actuators A: Physical **351**, 114171 (2023).
20. A. L. Eichhorn and C. Dietz, Advanced Materials Interfaces **n/a** (n/a), 2101288 (2021).
21. A. L. Eichhorn and C. Dietz, Scientific Reports **12** (1), 8981 (2022).
22. A. L. Eichhorn, M. Hoffer and C. Dietz, Carbon **200**, 124-133 (2022).
23. D. Martin-Jimenez, M. G. Ruppert, A. Ihle, S. Ahles, H. A. Wegner, A. Schirmeisen and D. Ebeling, Nanoscale **14** (14), 5329-5339 (2022).
24. Y. Yamada, T. Ichii, T. Utsunomiya, K. Kimura, K. Kobayashi, H. Yamada and H. Sugimura, Nanoscale advances **5** (3), 840-850 (2023).
25. T. Rodriguez and R. Garcia, Applied Physics Letters **84** (3), 449-551 (2004).
26. N. F. Martinez, S. Patil, J. R. Lozano and R. Garcia, Applied Physics Letters **89** (15), 153115 (2006).
27. S. D. Solares and G. Chawla, Measurement Science and Technology **21** (12), 125502 (2010).
28. J. R. Lozano and R. Garcia, Physical Review Letters **100**, 076102-076105 (2008).
29. V. G. Gisbert and R. Garcia, ACS Nano **15** (12), 20574-20581 (2021).
30. S. Santos, K. Gadelrab, T. Olukan, J. Font, V. Barcons and M. Chiesa, Applied Physics Letters **122** (7), 071603 (2023).
31. E. T. Herruzo, A. P. Perrino and R. Garcia, Nature Communications **5** (1), 3126 (2014).
32. A. Labuda, M. Kocuń, W. Meinhold, D. Walters and R. Proksch, Beilstein J Nanotechnol **7**, 970-982 (2016).

33. M. Kocun, A. Labuda, W. Meinhold, I. Revenko and R. Proksch, ACS Nano **11** (10), 10097-10105 (2017).
34. S. Benaglia, C. A. Amo and R. Garcia, Nanoscale **11** (32), 15289-15297 (2019).
35. V. G. Gisbert, S. Benaglia, M. R. Uhlig, R. Proksch and R. Garcia, ACS Nano **15** (1), 1850-1857 (2021).
36. A. Castellanos-Gomez, X. Duan, Z. Fei, H. R. Gutierrez, Y. Huang, X. Huang, J. Quereda, Q. Qian, E. Sutter and P. Sutter, Nature Reviews Methods Primers **2** (1), 58 (2022).
37. Y. Liu, Y. Huang and X. Duan, Nature **567** (7748), 323-333 (2019).
38. Y. Liu, N. O. Weiss, X. Duan, H.-C. Cheng, Y. Huang and X. Duan, Nature Reviews Materials **1** (9), 16042 (2016).
39. R. Frisenda, Y. Niu, P. Gant, M. Muñoz and A. Castellanos-Gomez, npj 2D Materials and Applications **4** (1), 38 (2020).
40. Z.-Y. Ong and M.-H. Bae, 2D Materials **6** (3), 032005 (2019).
41. Q. Zhang, G. Hu, W. Ma, P. Li, A. Krasnok, R. Hillenbrand, A. Alù and C.-W. Qiu, Nature **597** (7875), 187-195 (2021).
42. J. N. Israelachvili, *Intermolecular and Surface Forces*. (Elsevier Academic Press, London, 2005).
43. S. Santos, T. Olukan, L. Elsherbiny, A. Verdaguer and M. Chiesa, UiT Norges arktiske universitet https://munin.uit.no/handle/10037/26968 (2022).
44. B. Eslami, D. Ebeling and S. D. Solares, Beilstein J Nanotechnol **5**, 1144-1151 (2014).
45. R. Garcia and A. San Paulo, Physical Review B **60** (7), 4961 (1999).
46. R. Garcia, C. J. Gómez, N. F. Martinez, S. Patil, C. Dietz and R. Magerle, Physical Review Letters **97**, 016103-016104 (2006).
47. C.-Y. Lai, S. Perri, S. Santos, R. Garcia and M. Chiesa, Nanoscale **8** (18), 9688-9694 (2016).
48. M. D. Aksoy and A. Atalar, Physical Review B **83** (7), 075416 (2011).
49. S. Kawai, T. Glatzel, S. Koch, B. Such, A. Baratoff and E. Meyer, Physical Review Letters **103**, 220801-220804 (2009).
50. E. T. Herruzo and R. Garcia, Beilstein Journal of Nanotechnology **3**, 198-206 (2012).
51. C. Amo, Universidad Autónoma de Madrid, 2019.
52. V. G. Gisbert, C. A. Amo, M. Jaafar, A. Asenjo and R. Garcia, Nanoscale **13** (3), 2026-2033 (2021).
53. R. Takahashi and T. Okajima, Applied Physics Letters **107** (17), 173702 (2015).
54. S.-H. Oh, H. Altug, X. Jin, T. Low, S. J. Koester, A. P. Ivanov, J. B. Edel, P. Avouris and M. S. Strano, Nature Communications **12** (1), 3824 (2021).